JOURNAL OF CATALYSIS 156, 154–162 (1995)

Reduction Behavior of Metals Supported on Hydrous Titanium Oxide Ion-Exchange Materials

Allen G. Sault

Sandia National Laboratories, Fuel Science Department, MS 0710, Albuquerque, New Mexico 87185

Received January 25, 1995; revised April 18, 1995

Hydrous titanium oxide (HTO) ion-exchange materials provide a unique and versatile platform for obtaining high loadings of supported transition metal cations with essentially atomic dispersion. Strong interactions between the atomically dispersed metal cations and the support alter the reduction behavior of metal cations as compared to other support materials and preparation methods. X-ray photoelectron spectroscopy (XPS), Auger electron spectroscopy (AES), and secondary ion mass spectrometry (SIMS) measurements of the reduction of Rh, Ni, and Fe supported on HTO materials provide a representative cross section of possible behaviors. The results suggest that metals with high melting points and low surface mobility, such as Rh, Pt, and Pd, should retain high dispersions even after reduction at temperatures up to 300°C. Lower melting point metals such as Ni, Co, and Cu, that exhibit moderate heats of oxide formation, will likely undergo extensive sintering at temperatures above 250°C, largely negating the high dispersions characteristic of the freshly ion-exchanged state. Finally, lower melting point metals with very high heats of oxide formation, such as Fe and Cr, will be difficult to reduce due to unfavorable thermodynamics in the presence of the support. The results indicate that for certain types of metals, HTO support materials allow the preparation of catalysts with both high loadings and high metal dispersions. This capability provides a new pathway toward more efficient usage of expensive noble metals that is unavailable using conventional catalyst supports and preparation methods. © 1995 Academic Press, Inc.

1. INTRODUCTION

Using traditional supported metal catalyst preparation techniques, such as impregnation or incipient wetness, high metal dispersions can generally only be obtained at very low weight loadings. In contrast, hydrous titanium oxide (HTO) ion-exchange materials provide a potentially unique and versatile platform for the preparation of high loading, highly dispersed supported metal catalysts. Synthesized by the reaction of titanium isopropoxide with NaOH in methanol followed by hydrolysis (1, 2), HTO materials possess high surface areas (300 m^2/g), and high intrinsic cation-exchange capacities of up to 5 meq/g. This ion-exchange capacity allows for the possibility of obtaining high metal loadings with essentially atomic dispersion. Indeed, in the case of Ni^{2+} exchanged onto an HTO support, transmission electron microscopy (TEM) demonstrates that atomic or near-atomic dispersion can be achieved after ion exchange even for nickel loadings as high as 5–6% by weight (3, 4). Unfortunately, this high dispersion is largely lost during reduction (3, 4). Furthermore, Ni/HTO catalysts display unusual activation trends during hydrogen reduction (4), attributed to formation of an amorphous overlayer on the nickel particles during reduction. This overlayer, which consists of either carbonaceous residues or partially reduced titania (4–6), inhibits *n*-butane hydrogenolysis and its removal requires prolonged reduction at high temperatures (>350°C), or a short oxidation treatment after reduction. Surprisingly, oxidation prior to reduction results in a completely inactive catalyst (5), possibly because of an increased interaction between the nickel ions and the support that inhibits reduction (6). Surface analysis of Ni/HTO materials using Auger electron spectroscopy (AES) and secondary ion mass spectrometry (SIMS) supports the conclusions of the reactivity and TEM studies and also provides evidence for a phenomenon resembling a strong metal–support interaction (SMSI) at anomalously low temperatures (6). Although Ni/HTO catalysts do not appear to offer significant advantages over more conventionally prepared Ni/TiO_2 catalysts, the possibility exists that other transition metals supported on HTO materials will exhibit unique and advantageous properties relative to conventional titania supports, particularly if the high dispersions characteristic of the freshly ion-exchanged material can be retained following reduction of the metal. The possibility that HTO supports could allow the preparation of high-weight loading, highly dispersed catalysts therefore presents a potentially important new catalyst synthesis route that could lead to more efficient use of expensive noble metals. This manuscript presents a comparative study of the activation behavior of nickel, iron, and rhodium supported on HTO materials. Since several investigations of the Ni/HTO have already appeared (3, 4, 6), results for Ni/HTO will be presented first and compared with the earlier work. The results will then be extended to the Rh/HTO and Fe/HTO systems which have not been

0021-9517/95 $12.00

described previously. These three metals span a wide range of reducibility and as such provide a good basis for determining the range of activation behaviors possible with HTO supports.

2. METHODS

All experiments were performed in an ultra-high vacuum (UHV) chamber coupled to an atmospheric pressure reaction cell. This apparatus is identical to one described elsewhere (6), except that facilities for X-ray photoelectron spectroscopy (XPS) and ion scattering spectroscopy (ISS) have been added. A previous publication presents details of Auger electron spectroscopy and secondary ion mass spectrometry depth profile measurements (6). XPS was performed with a VG Microtech CLAM2 hemispherical analyzer operated at a pass energy of 50 eV and a slit width of 4 mm. A dual anode X-ray source oriented 50° away from the analyzer lens axis provided primary excitation. In order to avoid interference between the metal core levels of interest and the Auger transitions from other elements in the samples, a 300 W Mg$K\alpha$ source was used for Rh/HTO, while a 600 W Al$K\alpha$ source was used for Fe/HTO and Ni/HTO. The XPS energy scale was calibrated by measuring the positions of the Cu $2p_{3/2}$ (932.7 eV) and Cu $3p$ (75.1 eV) peaks from the copper sample holder (7). Both XPS and AES data are plotted by drawing straight lines between individual data points without any smoothing, background subtraction, or curve fitting.

Thin HTO films on tantalum foils provide an excellent platform for UHV studies as they are thick enough to completely attenuate signals from the tantalum substrate, yet thin enough that sample charging is largely avoided in AES, and can be accounted for in XPS by referencing all binding energies to the Ti $2p_{3/2}$ peak at 458.5 eV. An earlier publication (6) discusses the preparation of HTO films. At present, the morphology and thickness of these films is poorly characterized. Surface acoustic wave measurements of film surface areas (8) show that the total surface area of a ~50-nm-thick film is approximately twice the geometric surface area, but it is unclear whether porosity, cracks in the films, or surface roughness lead to this excess surface area. SEM images of the films indicate that the film surfaces are smooth and dense on the submicrometer scale, except for some cracking and delamination of the films from the tantalum substrate caused by shrinking of the film during drying. Although these films do not exhibit the high surface areas typical of bulk HTO materials, earlier AES and SIMS results on Ni/HTO (6) strongly suggest that the reduction behaviors of metals supported on HTO films closely approximate those of the bulk materials. Furthermore, analysis of thin films is directly relevant to the practical use of HTO materials as catalyst supports, since cost considerations may prevent the use of bulk HTO materials and require thin-film HTO materials deposited on inexpensive, high surface area, oxide substrates.

The films are loaded with the metals of interest via an ion-exchange process. For each metal, several foils were exchanged simultaneously in order to provide a consistent set of samples. Iron was loaded as Fe^{2+} by first equilibrating the foils for several hours in deionized water adjusted to pH 5.4 using dilute nitric acid, and then rapidly transferring the foils to a 0.025 M solution of $FeCl_2$ (Fisher, certified), also adjusted to pH 5.4. After several hours, the pH dropped to 4.2 and stabilized. The foils were then rinsed with deionized water and allowed to dry in air. The iron loading depends very sensitively on ion-exchange conditions (9), and variations of a factor of 2–3 in the loading were observed for nominally identical loading conditions. Results for the foils with the lowest iron loading are presented here in order to maximize the probability that the iron is loaded by ion-exchange rather than precipitation. Nickel was loaded in a manner similar to iron, but using a 0.0055 M $Ni(NO_3)_2$ solution at a pH of ~5.2 (6). Rhodium loading was performed by equilibrating the coated foils in 100 ml deionized water at pH 4.0, followed by addition of 33 μl of a 0.03 M $Rh(NO_3)_3$ (Johnson Matthey, 99.9%) solution. Rhodium loading requires a lower pH than either nickel or iron in order to avoid hydrolysis reactions and precipitation of insoluble hydroxides during ion exchange. Also, the rhodium concentration (10^{-5} M) is much lower than for nickel or iron. Higher rhodium concentrations result in extremely high rhodium signals in AES and XPS and introduce the possibility that some of the rhodium is loaded by precipitation rather than ion exchange. As with the Fe/HTO samples, results for the lowest rhodium loading samples are presented in order to ensure that the results are characteristic of rhodium loaded by ion exchange only.

In situ reduction and oxidation treatments took place in the atmospheric pressure reaction cell coupled to the UHV chamber. All treatments were done in a batch mode by ramping the sample to the desired temperature under vacuum, filling the reactor with the desired pressure of gas, heating for the specified time, and then evacuating the reactor while holding the sample at temperature. Further details on the reduction and oxidation procedures are given elsewhere (6). Research-purity gases were used for all activation treatments. No further purification was performed for any of the gases, except CO. Metal carbonyls were removed from the CO by passing the gas through a glass-wool-packed U tube immersed in liquid nitrogen.

3. RESULTS

3.1. Ni/HTO

Figure 1 shows representative XPS results for the Ni/HTO films. Initially, the nickel is present mainly as Ni^{2+}, as demonstrated by the position of the Ni $2p_{3/2}$ peak

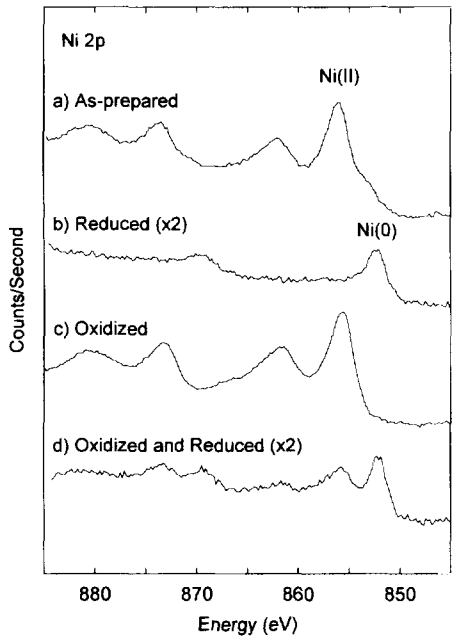

FIG. 1. Ni 2*p* XPS of Ni/HTO films: (a) in the as-prepared state; (b) after reduction under 5 Torr H_2 at 350°C for 2 h; and (c) after subsequent oxidation under 130 Torr O_2 at 300°C for 2 h. Spectrum (d) shows the Ni 2*p* region after oxidation of an as-prepared Ni/HTO film under 130 Torr O_2 at 300°C for 2 h, and subsequent reduction under 5 Torr H_2 at 350°C for 2 h. Intensities are normalized to the Ti 2*p* peak areas.

at 856.0 eV and the characteristic shake-up feature at 862.2 eV (10, 11). Because the presence of shake-up features and a large background change through the Ni 2*p* region make determination of the Ni $2p_{3/2}$ peak area difficult, no quantitative analysis of the Ni/HTO XPS data was attempted. Previous analysis of AES data for Ni/HTO (6) gave a nickel loading of ~5% by weight, in good agreement with elemental analysis of bulk HTO materials prepared in a similar manner (3, 4).

Heating the Ni/HTO film under either vacuum or 5 Torr H_2 at 300°C or greater results in quantitative reduction of the nickel to the metallic state, as evidenced by the shift of the Ni $2p_{3/2}$ peak to 852.3 eV and the loss of the shake-up intensity. A substantial decrease in intensity of the Ni 2*p* peaks relative to the Ti 2*p* peaks occurs during reduction. Reoxidation of the Ni/HTO film in 130 Torr O_2 at 300°C completely restores the nickel to the +2 state, and also results in a substantial increase in the Ni 2*p* intensity to a level approaching that of the freshly ion-exchanged film. The changes in Ni 2*p* intensity with reduction and oxidation are entirely consistent with earlier AES/SIMS results on Ni/HTO films (6). Reduction of the nickel upon heating in vacuum is attributed to the presence of carbonaceous residue in the freshly prepared films that provides the reducing equivalents, while the decrease in the Ni signal in both AES and XPS arises from the formation of large (10–20 nm) metallic nickel particles from the initially atomically dispersed nickel ions. The increase in signal upon reoxidation is attributed mainly to removal of the amorphous overlayer discussed in the Introduction, but could also be evidence for an SMSI effect.

The complete reduction of nickel contrasts with earlier measurements that used oxygen uptake following reduction to determine the extent of reduction in bulk Ni/HTO (3, 6). These studies conclude that only one-third of the nickel can be reduced in hydrogen at temperatures up to 400°C. The XPS results clearly demonstrate that all of the nickel in the near-surface region of the films is reduced and therefore suggest that the lack of complete reduction in bulk Ni/HTO materials may be due to physical changes in the support during reduction that prevent access of gas-phase reactants to a portion of the nickel. Surface area losses during reduction (5, 12) are consistent with this explanation, although surface area loss is minor below 350°C. The diffusion of a large fraction of the Ni^{2+} ions into the HTO matrix (5, 13) provides a second possible explanation for the absence of any unreduced nickel in the XPS spectrum, although it is difficult to imagine that the nickel ions would diffuse far enough below the surface so that the Ni^{2+} photoelectrons would be completely attenuated. Finally it is possible that the reduction behavior of Ni/HTO films differs from bulk Ni/HTO, although in all other respects the two systems behave similarly.

In order to assess earlier work (6), which speculated that oxidation of Ni/HTO prior to reduction alters the interaction of the nickel ions with the support, a freshly prepared Ni/HTO sample was oxidized at 300°C under 130 Torr O_2 for 2 h, then reduced at 350°C under 5 Torr H_2 for 2 h. Oxidation resulted in removal of adventitious carbon, but no changes in the Ni 2*p* XPS spectrum. After reduction, Ni $2p_{3/2}$ peaks are evident at 852.1 eV (metallic nickel), and at 855.7 and 861.5 eV (Ni^{2+}) (Fig. 1d). Thus, under conditions that result in complete reduction of freshly prepared Ni/HTO, preoxidized Ni/HTO undergoes only partial reduction. Furthermore, the loss in Ni 2*p* intensity upon reduction is lower for the oxidized sample than for the as-prepared sample, in agreement with earlier AES measurements (6). The true extent of reduction of the oxidized sample may be overestimated by these experiments since some reduction occurs during the installation of the sample. This reduction results from heating the reactor to ~80°C after sample installation to remove water from the reactor walls and improve the ultimately attainable vacuum. That this treatment causes some reduction is clear from the small shoulder on the low binding energy side of the Ni $2p_{3/2}$ peak in Fig. 1a. The fraction of the nickel that is reduced prior to the initial oxidation treatment most likely forms large particles that oxidize and reduce easily. The remainder of the nickel is apparently more difficult to reduce, however, providing clear evidence that oxidation

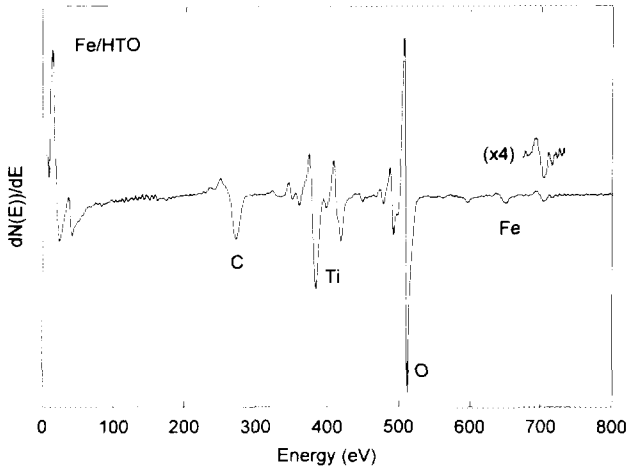

FIG. 2. AES of Fe/HTO film in the as-prepared state.

of Ni/HTO prior to reduction alters the interaction between the nickel ions and the HTO support, thereby decreasing the reducibility of the nickel and resulting in negligible activity for *n*-butane hydrogenolysis (5).

3.2. Fe/HTO

Figure 2 shows a typical Auger spectrum of an Fe/HTO foil. The spectrum shows Ti, O, and Fe as expected, along with a relatively large carbon peak resulting from organic residues deposited in the film during preparation. The Fe(703 eV)/Ti(384 eV) ratio is approximately 0.07, vs 0.04 for the Ni(848 eV)/Ti(384 eV) ratio in Ni/HTO (6). Accounting for relative AES sensitivity factors for nickel (0.26) and iron (0.21) (14), and an earlier analysis showing that the Ni(848 eV)/Ti(384 eV) ratio of Ni/HTO corresponds to a loading of ~5% by weight (6), the iron loading can be estimated to be approximately 10% by weight. Based on a nominal, volatile free, Na/HTO composition of $NaTi_2O_5H$ (1, 2), the maximum iron loading obtainable by ion exchange of Fe^{2+} is 14%. Thus, it is possible that all of the iron was loaded by ion-exchange, although the presence of some precipitated iron cannot be ruled out.

XPS of the Fe/HTO sample is shown in Fig. 3. For the freshly ion-exchanged sample, the position of the Fe $2p_{3/2}$ peak at 709.8 eV and the characteristic shake-up feature ~715 eV clearly identify the iron oxidation state as +2, as expected (15). Quantitative analysis of Fe 2*p* XPS suffers from the same difficulties as described for Ni 2*p*, and therefore was not attempted. Treatment of the Fe/HTO film in 5 Torr of hydrogen at temperatures up to 400°C results in a narrowing of the Fe 2*p* features but no evidence for any metallic iron. The narrowing is attributed to slight reduction of the titania support, which decreases sample charging and thereby minimizes the effects of differential charging on XPS peak widths. Evidence for titania reduction comes from subtle changes in the Ti (LMV) Auger lineshape during hydrogen treatment, similar to those observed for Ni/HTO (6). No evidence for Ti^{3+} appears in the Ti 2*p* XPS spectrum, indicating that AES is a more sensitive qualitative indicator of titania reduction than XPS.

The size of the Fe $2p_{3/2}$ peak in the ion-exchanged sample decreases by less than 25% relative to the Ti 2*p* peaks during hydrogen treatment, contrasting with the large attenuation of the Ni 2*p* signal upon reduction of Ni/HTO. AES also detects little change in the iron signal upon hydrogen treatment. In the absence of iron reduction, formation of large iron particles does not occur and consequently little change in the Fe 2*p* signal intensity is observed. The small reduction in Fe 2*p* intensity may result from diffusion of iron ions into the HTO matrix to form iron titanate structures (e.g., ilmenite ($FeTiO_3$)).

The failure of hydrogen treatments to reduce the Fe^{2+} in Fe/HTO led to attempts to reduce the iron using carbon monoxide, since the thermodynamics of iron reduction are much more favorable in CO than in hydrogen (16). Treatment under 100 Torr CO at 350–400°C for 2 h results in formation of zerovalent iron from about 10–20% of the total iron present. This zerovalent iron appears as a low-energy shoulder in Fig. 3c, with a binding energy of ~707.5 eV estimated by subtraction of the Fe 2*p* spectrum of the freshly prepared Fe/HTO. The uncertainties associ-

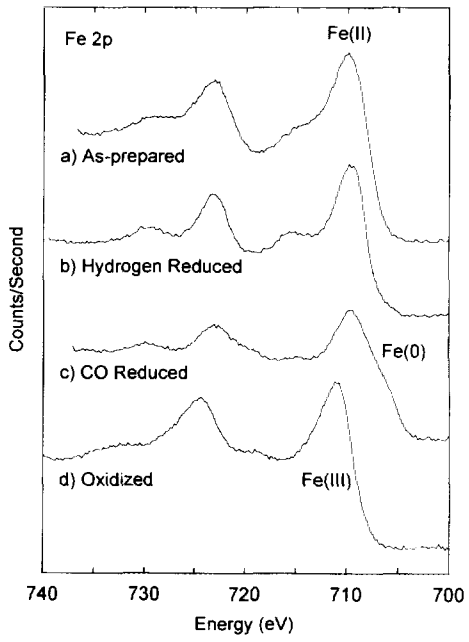

FIG. 3. Fe 2*p* XPS of Fe/HTO film: (a) in the as-prepared state; (b) after reduction under 5 Torr H_2 at 350°C for 2 h; (c) after reduction under 100 Torr CO at 400°C for 2 h. Spectrum (d) shows the Fe 2*p* region after oxidation of a Fe/HTO foil under 130 Torr O_2 at 300°C for 2 h. Intensities are normalized to the Ti 2*p* peak areas.

ated with this subtraction and with charge referencing to the Ti $2p_{3/2}$ peak prevent discrimination between metallic iron and iron carbide, which differ by only 0.3 eV in the Fe $2p_{3/2}$ binding energy (15, 17). Since iron carbide is easily formed by reaction of metallic iron with CO at 350–400°C (15, 17), assignment of the low binding energy shoulder to a carbide seems most likely. As with hydrogen treatment, little or no change in the intensity of the Fe 2*p* XPS or Fe (703 eV) AES signals occurs during CO treatment. The small fraction of iron which reduces in CO, and presumably forms iron carbide particles, is insufficient to significantly decrease the total iron signal.

Although the Fe^{2+} ions in Fe/HTO resist reduction, oxidation to Fe^{3+} is facile. Oxidation under 130 Torr O_2 at 300°C for 2 h quantitatively converts Fe^{2+} to Fe^{3+} as evidenced by shifts in the Fe $2p_{3/2}$ peak and the shake-up feature to 711.0 eV and ~719 eV, respectively (15) (Fig. 3d). Subsequent treatment in 5 Torr H_2 at 350°C for 2 h reduces the Fe^{3+} back to Fe^{2+}, but not to metallic iron. The thermodynamics of the Fe/HTO system are therefore such that conversion between Fe^{2+} and Fe^{3+} is favorable, but reduction to the metal is not.

3.3. *Rh/HTO*

Due to the ease with which rhodium can be reduced, it is difficult to obtain either XPS or AES of freshly prepared Rh/HTO. Bombardment of the surface with stray electrons generated by the ion gauge filament, or with secondary electrons generated during AES can result in complete reduction of the rhodium. Even a system bakeout at 80°C to obtain ultra-high vacuum results in substantial reduction. Figure 4 shows the Rh 3*d* spectrum obtained from a Rh/HTO sample installed in the reactor and pumped overnight without bakeout before introduction into the analysis chamber. The Rh $3d_{5/2}$ peak appears at 309.5 eV, indicating that the vast majority of the rhodium is in the +3 oxidation state (10, 11). Even here, however, a small shoulder is apparent near 307.5 eV corresponding to metallic rhodium. Heating to 150°C in vacuum completely reduces the rhodium to the metallic state. The Rh $3d_{5/2}$ peak narrows and shifts to 307.5 eV and decreases slightly in size relative to the Ti 2*p* peaks. As for Ni/HTO (6), reduction of Rh/HTO under vacuum is attributed to organic residue present in the HTO materials. Continued heating under vacuum results in further decreases in the Rh 3*d* intensity and binding energy. After heating to 300°C under 5 Torr H_2 for 2 h, the Rh 3*d* intensity falls to about 60% of the initial value and the Rh $3d_{5/2}$ binding energy decreases to 306.8 eV.

The changes in the Rh 3*d* region upon reduction undoubtedly arise from rhodium particle growth, although the changes are much less severe than those observed upon reduction of Ni/HTO. Assuming that the freshly prepared

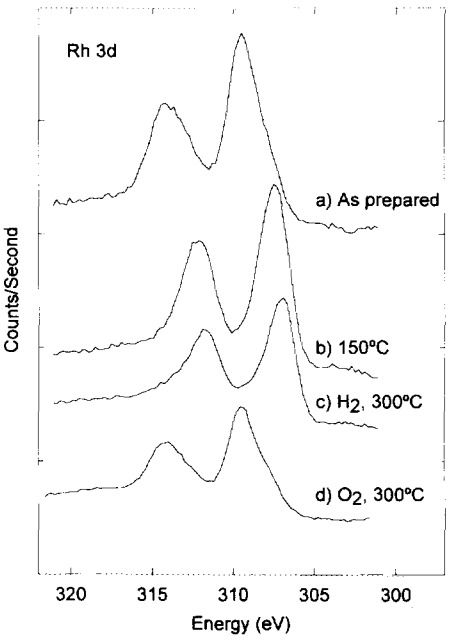

FIG. 4. Rh 3*d* XPS of Rh/HTO film: (a) in the as-prepared state; (b) after heating to 150°C under vacuum; (c) after reduction under 5 Torr H_2 at 300°C for 2 h; (d) after oxidation of the reduced film under 130 Torr O_2 at 300°C for 1 h. Intensities are normalized to the Ti 2*p* peak areas.

Rh/HTO samples contain atomically or nearly atomically dispersed Rh^{3+} ions, the relatively small decrease in Rh 3*d* intensity upon reduction indicates that small Rh particles are formed with diameters on the order of the attenuation length (AL) of Rh 3*d* photoelectrons. Since the AL of Rh 3*d* photoelectrons is approximately 1.5 nm (18), the metallic rhodium particles must be only a few nanometers in diameter. Quantitative analysis of the Rh/HTO XPS data agrees well with the postulated formation of small particles (unlike Ni 2*p* and Fe 2*p*, quantitative XPS analysis of the Rh 3*d* region is reliable since there are no complications due to shake-up features or large background changes). The analysis, performed in a manner described by Seah (19), assumes a flat, dense film surface as observed by SEM, and uses XPS sensitivity factors measured by Wagner *et al.* (20) and ALs taken from Seah and Dench (18). Since Wagner *et al.* report only sensitivity factors for the elements, the relative Ti 2*p* intensity expected from TiO_2 must first be calculated using the equations for homogeneous binary samples (19). Next, based on the SIMS depth profile data presented below, all of the rhodium is taken to be on the surface of the HTO film, and is further assumed to be atomically dispersed initially. Using the appropriate equations for an homogeneous sample with fractional monolayer coverage (19), and inserting the measured Rh 3*d*/Ti 2*p* intensity ratio of ~0.23 for the as-prepared film, gives a fractional surface coverage of 0.45

monolayers of rhodium. Based on this coverage, the particle size necessary to obtain the final Rh 3*d*/Ti 2*p* intensity ratio of 0.13 following reduction under H_2 at 300°C can be determined, and turns out to be ~2 nm. Following the less-severe reduction treatment of heating to 150°C in vacuum, the particles must be even smaller based on the higher Rh 3*d*/Ti 3*p* intensity ratio. Hydrogen uptake and TEM measurements on bulk Rh/HTO materials, to be reported elsewhere, support the presence of small, 2- to 4-nm particles (5, 13). The apparent small rhodium particle size in reduced Rh/HTO contrasts with the large, 10- to 20-nm nickel particles formed upon reduction of Ni/HTO, indicating that the very high dispersion characteristic of ion-exchanged metal ions supported on HTO materials can be retained in Rh/HTO materials after reduction.

The sintering of small rhodium particles explains the observed shifts in the Rh $3d_{5/2}$ binding energy as the reduction temperature increases. Following emission, the kinetic energy of the photoelectron is determined in part by the extent to which the atomic core hole in the final state is screened by extra-atomic relaxation of electrons from the valence band of the metal particle. This screening decreases the final state energy of the core hole, and thereby increases the amount of energy available to photoelectron. This effect is small or negligible for isolated metal atoms or very small metal particles, and increases with particle size, eventually reaching the bulk value (21, 22). Consequently, for particles small enough that the electronic structure differs from the bulk, photoelectron kinetic energies increase (i.e., binding energies decrease) with particle size, as observed here.

Unlike with nickel, in which an oxidation treatment following reduction restores the nickel signal to values approximating those of the freshly prepared Ni/HTO, oxidation of Rh/HTO at 300°C following reduction results in a further decrease in the Rh 3*d* signal. Figure 4d shows that this decrease is accompanied by nearly complete oxidation of the rhodium metal to the +3 state, indicating Rh_2O_3 formation. Subsequent reduction converts the rhodium back to the metallic state with little change in Rh 3*d* signal intensity. For Ni/HTO, large increases in nickel XPS and AES intensities upon oxidation are attributed to removal of the amorphous overlayer described earlier, and oscillations in the Ni/Ti ratios during subsequent reduction/oxidation cycles have elsewhere been shown (6) to be due to a low-temperature SMSI effect. The differing behavior of Rh/HTO suggests that such phenomena are absent or much less important for Rh/HTO. Instead, it appears that both oxidation and reduction of Rh/HTO cause mild sintering of rhodium particles.

3.4. Depth Profiling

SIMS depth profiles of freshly prepared Ni/HTO, Fe/HTO, and Rh/HTO films are presented in Fig. 5. The

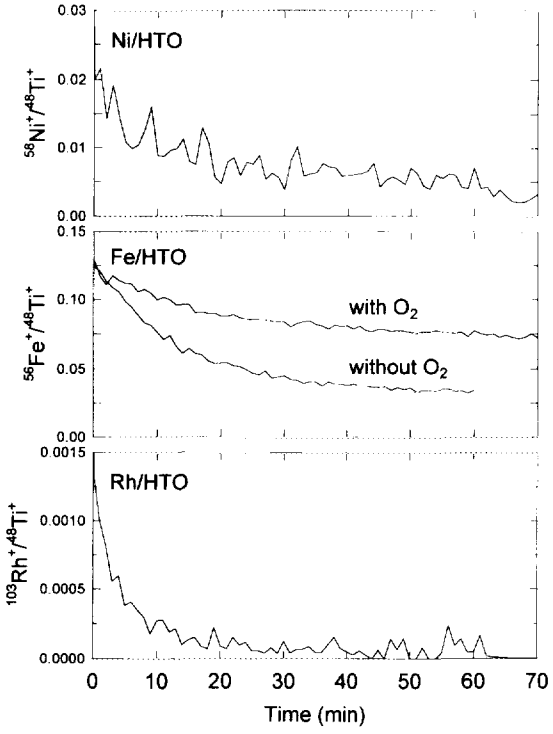

FIG. 5. SIMS depth profiles from Ni/HTO, Fe/HTO, and Rh/HTO films. Data were taken using 3 keV argon ions with an ion flux of 1.5×10^{13} ions/cm^2/s. Depth profiles of Fe/HTO were taken both with and without a background pressure of 10^{-7} Torr O_2 to suppress reduction of the HTO support.

depth profiles for Ni/HTO and Fe/HTO are very similar; the $^{58}Ni^+/^{48}Ti^+$ and $^{56}Fe^+/^{48}Ti^+$ SIMS ratios decrease by a factor of 4–5 with depth. Auger spectra taken from the sputter craters after the depth profiles indicate substantial reduction of titania, but no decreases in the Ni(848 eV)/Ti(384 eV) or Fe(703 eV)/Ti(384 eV) ratios. This apparent discrepancy between SIMS and AES is reconciled by assuming that changes in the ion yield of the various secondary ions occur with titania reduction (6). These changes, an example of the SIMS matrix effect (23), result in a decrease in the $^{58}Ni^+/^{48}Ti^+$ and $^{56}Fe^+/^{48}Ti^+$ SIMS ratios even though the actual concentrations of nickel and iron in the films do not change with depth. By backfilling the vacuum chamber with 10^{-7} Torr O_2 during a depth profile of Fe/HTO, sputter-induced reduction of the HTO material can be largely prevented, resulting in only a 30–40% decrease in the $^{56}Fe^+/^{48}Ti^+$ SIMS ratio with depth.

The behavior of Rh/HTO is qualitatively different from Ni/HTO and Fe/HTO. In Rh/HTO the $^{103}Rh^+/^{48}Ti^+$ SIMS ratio rapidly decreases to zero with depth. Auger spectra taken from the sputter crater indicate a complete absence of rhodium inside the HTO film. Thus, unlike Ni/HTO and Fe/HTO, the observed decrease in the $^{103}Rh^+/^{48}Ti^+$ SIMS ratio accurately reflects changes in the rhodium con-

centration with depth. This observation provides further evidence that the loading of Rh^{3+} ions onto HTO supports is qualitatively different from the loading of Ni^{2+} and Fe^{2+}. While both Ni^{2+} and Fe^{2+} ions can penetrate the film, either due to porosity in the film or to an ability of these ions to diffuse through the dense HTO matrix during ion-exchange, Rh^{3+} ions are unable to penetrate and therefore are loaded only on the film surface. A possible explanation for this difference is that the solution chemistry of Rh^{3+} may favor the formation of large oxyhydroxide clusters which are too large to penetrate any pores present in the films, or are unable to diffuse through the HTO matrix. Unfortunately, little information is available in the literature regarding Rh^{3+} solution chemistry.

For Fe/HTO and Rh/HTO films the depth profiles are insensitive to either reduction or oxidation treatments. In the case of Ni/HTO, reduction substantially decreases the initial $^{58}Ni^+/^{48}Ti^+$ SIMS ratio (6). This decrease results from the formation of large nickel particles during reduction, which decreases the fraction of the film surface covered by nickel atoms. The absence of significant changes in the Fe/HTO and Rh/HTO depth profiles with reduction is consistent with the lack of iron reduction in Fe/HTO and the formation of small rhodium particles in Rh/HTO. In both cases, the fraction of the film surface covered by the metal atoms does not change significantly, and this fact is reflected in SIMS as well as XPS and AES.

4. DISCUSSION

For reactions which are structure insensitive, the ability to prepare supported metal catalysts with high dispersions even at high loadings would result in extremely efficient usage of noble metals. The inherent ion-exchange capacity of HTO materials provides a potentially important synthesis method for achieving this goal. Although these materials allow the loading of metal ions with essentially atomic dispersion, agglomeration of the metal ions during reduction remains problematic. TEM, XPS, AES, and chemisorption (3–6) all reveal that severe agglomeration of nickel occurs upon reduction of Ni/HTO containing ~6.0 wt% nickel. The initial atomic dispersion is completely lost and particles on the order of 10–20 nm form. For both Fe/HTO and Rh/HTO, however, XPS and AES strongly suggest that little agglomeration of these metals occurs during reduction. In the case of Fe/HTO, the absence of agglomeration is related to the absence of iron reduction. Without reduction, the iron ions remain tightly bound to the ion-exchange sites and diffusion to form large particles is highly activated. Thus, although Fe/HTO retains the high dispersion that characterizes the freshly prepared catalysts, no metallic iron forms, and activity for reactions which are catalyzed by metallic iron is expected to be negligible. Tests of Fe/HTO catalysts for Fischer–Tröpsch synthesis confirm this expectation (24). Fe/HTO materials may, however, exhibit high activities for reactions such as selective dehydrogenation, which are catalyzed by iron oxides. Experiments using Fe/HTO to catalyze ethylbenzene dehydrogenation to styrene indicate that Fe/HTO is, in fact, an active catalyst for this reaction (9).

For Rh/HTO, complete reduction to the metal is facile, but unlike Ni/HTO, occurs without extensive particle growth. This result might be expected for very low reduction temperatures where metal atom diffusion rates are slow, but it is quite unexpected following reduction at higher temperatures. Two primary mechanisms for sintering are migration and coalescence of metal particles, and emission of atoms from small particles and capture by larger particles (Ostwald ripening) (25). Both of these mechanisms for sintering qualitatively predict a lower rate of sintering for high melting point metals such as rhodium than for lower melting point metals such as nickel. For Ni/HTO, the relatively high sintering rate overcomes the initial atomic dispersion and results in large particles. For Rh/HTO, however, the initial atomic dispersion of the rhodium ions following ion exchange, coupled with a low sintering rate, results in the formation of only small, highly dispersed rhodium particles even at high metal loadings. Preparation of high weight loading supported rhodium catalysts by other catalyst preparation techniques, such as wet impregnation followed by calcining in air, generally results in the formation of large rhodium oxide particles even before reduction. As a result, large metal particles are likely to be formed during reduction.

Regardless of the explanation for the lower sintering rate of rhodium relative to nickel, the Rh/HTO experiments demonstrate that high dispersions can be obtained on HTO supports even at high metal loadings. Chemisorption, TEM, and catalytic activity studies by Gardner *et al.* (5, 13) conclusively demonstrate the presence of small rhodium particles in reduced Rh/HTO. This important result highlights the unique nature of HTO ion-exchange materials as catalyst supports. Assuming that the simple explanation given above for the sintering resistance of Rh/HTO is correct, then other metals with high melting points, such as Pt and Pd, should also display stable high dispersions at high loadings on HTO supports. It is important to note that the sintering rate arguments given above apply equally well to more conventional supports, such as silica and alumina, as to HTO materials. The unique aspect of HTO ion-exchange materials is that high metal dispersions at high metal loadings can be achieved prior to reduction by proper control of ion-exchange conditions. It is this property of HTO materials that allows the sintering resistance of certain metals to be utilized to obtain highly dispersed, highly loaded supported metal catalysts even after reduction.

The complete absence of reduction of iron during hydro-

gen treatment of Fe/HTO requires some explanation since the reduction conditions tested are sufficient to reduce bulk iron oxide to the metal (26, 27). (Note that temperature-programmed reduction (TPR) studies that observe complete reduction to iron only at temperatures well above 400°C (26, 28) are not necessarily indicative of the reduction temperatures required under isothermal conditions (26)). Water outgassed from the sample during the batch reduction might be expected to inhibit or reverse reduction somewhat, but it is unlikely that this water would completely prevent iron reduction. An estimate of the H_2O/H_2 ratio in the reactor at the end of a reduction treatment, based on the measured water pressure with the sample at temperature, the known pumping speed of the chamber, the reactor volume, and the reduction time, gives a value of 0.072. Since this estimate is lower than the equilibrium constant (K_{eq} = 0.107) for the reduction of magnetite to metallic iron (16), the presence of water in the reactor cannot account for the complete absence of iron reduction. Instead, interactions between Fe^{2+} and the HTO support most likely explain the complete absence of iron reduction. Available literature (29–32) on supported iron clearly demonstrates that the extent of reduction depends on both support identity and preparation, although a complete absence of metallic iron is rare. The highly dispersed nature of the iron ions in the ion-exchanged Fe/HTO, as opposed to deposition in clusters containing multiple iron ions and counterions, such as that which occurs during loading of iron by wet impregnation methods, may very well serve to increase the strength of interaction between the iron and the support, thereby severely limiting reduction to the metal.

The trend in reducibility for Rh, Ni, and Fe supported on HTO materials agrees well with recent work by Madey and co-workers [33–35], which shows that the strength of interaction of vapor deposited metals on TiO_2(110) surfaces increases with the heat of formation of the metal oxide. Furthermore, for metals such as iron and chromium that have high heats of oxide formation, reduction of the TiO_2 support can occur during deposition of the first monolayer, resulting in an oxidized metal overlayer supported on a partially reduced TiO_2 substrate. The relative reducibilities of Rh, Ni, and Fe/HTO materials exactly agrees with the heats of oxidation, and the inability to reduce Fe/HTO even at 400°C is entirely consistent with the observed ability of metallic iron to reduce titania. To a limited extent, it may be that some metallic iron forms during hydrogen reduction of Fe/HTO, but is rapidly reoxidized by the titania support. The absence of substantial Ti^{3+} formation during reduction suggests, however, that the amount of iron which undergoes this process is minor. Within this context, the small amount of iron reduction which is seen in a carbon monoxide atmosphere can be explained. In the presence of CO, any iron which is reduced can not only be reoxidized by the support, but can further react with CO to form the carbide. If reoxidation of the carbide by the support is less favorable than reoxidation of metallic iron, then any carbide formed would be expected to be more stable than metallic iron, as observed.

5. CONCLUSIONS

The comparative behavior of Rh, Ni, and Fe supported on HTO ion-exchange materials demonstrates important trends in the activation behavior of HTO-supported metals. For rhodium, reduction to the metal is facile and occurs without agglomeration of the rhodium into large particles. In contrast, reduction of Ni/HTO requires fairly high temperatures and results in formation of large metallic nickel particles, while reduction of Fe/HTO in hydrogen is not possible at all at temperatures up to 400°C. The trends in reduction behavior are related to both the heats of formation of the metal oxides and the mobility of metal atoms on the surface. For high melting point metals such as Rh, mobility is low and sintering is therefore slow. Coupled with an initial atomic dispersion of the ion-exchanged metal anions, the low mobility results in formation of only small, highly dispersed metal particles even at high metal loadings. In contrast, metals which are fairly easy to reduce, but have relatively low melting points, such as nickel, form large particles during reduction and the atomic dispersion characteristic of the freshly ion-exchanged material is largely lost. Finally, for metals such as iron, which have high heats of oxide formation, reduction to the metal is not possible even at temperatures that are sufficient to reduce the bulk metal oxide. This behavior arises from a strong interaction between the HTO support and the iron ions, as well as unfavorable thermodynamics for iron reduction on titania surfaces. Based on these results, the activation behavior of other metals supported on HTO materials can be predicted. High melting point metals, such as Pt and Pd, are predicted to form small highly dispersed metal particles on HTO supports, even at high metal loadings, while low melting point metals with moderate heats of oxide formation, such as Cu and Co, are expected to sinter to form large metal particles. Metals with extremely high heats of oxide formation, such as Fe and Cr, are not expected to undergo reduction at all due to strong interactions with the HTO support. Thus, the unique ion-exchange properties of HTO materials, which allow high metal loadings to be achieved with essentially atomic dispersion in the freshly ion-exchanged state, result in highly dispersed, high-loading catalysts after reduction for certain classes of metals. This capability allows more efficient usage of expensive noble metals at high loadings than can be achieved with conventional support materials and standard catalyst preparation techniques.

ACKNOWLEDGMENTS

The author gratefully acknowledges support for this work from the Department of Energy, Fossil Energy Materials Program. The author thanks Tony Ricco for performing the surface acoustic wave measurements, and Abhaya Datye for providing SEM images. Helpful discussions with Tim Gardner and Kent Coulter are also gratefully acknowledged.

REFERENCES

1. Dosch, R. G., Stephens, H. P., Stohl, F. V., Bunker, B. C., and Peden, C. H. F., "Hydrous Metal Oxide-Supported Catalysts: Part I. Preparation Chemistry and Physical and Chemical Properties," Sandia Report SAND89-2399. Sandia National Laboratories, Albuquerque, NM, 1990. [Available from National Technical Information Service, U.S. Department of Commerce, 5285 Port Royal Road, Springfield, VA 22161]
2. Stephens, H. P., and Dosch, R. G., *in* "Preparation of Catalysts IV" (B. Delmon, P. Grange, P. A. Jacobs, and G. Poncelet, Eds.), p. 271. Elsevier, Amsterdam, 1987.
3. Anderson, S. L., Datye, A. K., Braunschweig, E. G., and Peden, C. H. F., *Appl. Catal.* **82,** 185 (1992).
4. Gardner, T. J., Peden, C. H. F., and Datye, A. K., *Catal. Lett.* **15,** 111 (1992).
5. Gardner, T. J., Ph.D. thesis, University of New Mexico, 1994.
6. Sault, A. G., Boespflug, E. P., and Peden, C. H. F., *J. Phys. Chem.* **98,** 1652 (1994).
7. Anthony, M. T., and Seah, M. P., *Surf. Interface Anal.* **6,** 107 (1984).
8. Ricco, A. J., Frye, G. C., and Martin, S. J., *Langmuir* **5,** 273 (1989).
9. Boespflug, E. P., Coulter, K. E., and Sault, A. G., in preparation.
10. Wagner, C. D., Riggs, W. M., Davis, L. E., Moulder, J. F., and Muilenberg, G. E., "Handbook of X-ray Photoelectron Spectroscopy." Perkin–Elmer Corp., Eden Prairie, MN, 1979.
11. "Practical Surface Analysis by Auger and X-Ray Photoelectron Spectroscopy" (D. Briggs and M. P. Seah, Eds.), Appendix 4. Wiley, New York, 1983.
12. Bunker, B. C., Peden, C. H. F., Martinez, S. L., Braunschweig, E. J., and Datye, A. K. *in* "Characterization and Catalyst Development: An Interactive Approach" (S. A. Bradley and R. J. Bertalocini, Eds.), p. 65. Am. Chem. Soc., Washington, DC, 1989.
13. Gardner, T. J., and Datye, A. K., in preparation.
14. Davis, L. E. McDonald, N. C., Palmberg, P. W., Riach, G. E., and Weber, R. E., "Handbook of Auger Electron Spectroscopy." Perkin–Elmer Corp., Eden Prairie, MN, 1978.
15. Kuivila, C. S., Butt, J. B., and Stair, P. C., *Appl. Surface Sci.* **32,** 99 (1988).
16. Storch, H. H., Gulombic, N., and Anderson, R. B., "The Fischer-Tröpsch and Related Syntheses," p. 28 ff. Wiley, New York, 1951.
17. Dwyer, D. J., and Hardenberg, J. H., *J. Catal.* **89,** 66 (1984).
18. Seah, M. P., and Dench, W. A., *Surface Interface Anal.* **1,** 2 (1979).
19. Seah, M. P., *Surface Interface Anal.* **2,** 222 (1980).
20. Wagner, C. D., Davis, L. E., Zeller, M. V., Taylor, J. A., Raymond, R. H., and Gale, L. H., *Surface Interface Anal.* **3,** 211 (1981).
21. "Practical Surface Analysis by Auger and X-Ray Photoelectron Spectroscopy" (D. Briggs and M. P. Seah, Eds.), p. 96. Wiley, New York, 1983.
22. Mason, M. G., and Baetzold, R. C., *J. Chem. Phys.* **64,** 271 (1976).
23. Benninghoven, A., Rüdenauer, F. G., and Werner, H. W., "Secondary Ion Mass Spectrometry," p. 186. Wiley, New York, 1987.
24. Jackson, N. B., unpublished results.
25. Ruckenstein, E., *in* "Metal-Support Interactions in Catalysis, Sintering, and Redispersion" (S. A. Stevenson, J. A. Dumesic, R. T. K. Baker, and E. Ruckenstein, Eds.), p. 141 ff. Van Nostrand–Reinhold, New York, 1987.
26. Leith, I. R., and Howden, M. G., *Appl. Catal.* **37,** 75 (1988).
27. Richard, M. A., Soled, S. L., Fiato, R. A., and DeRites, B. A., *Mater. Res. Bull.* **18,** 829 (1983).
28. Hughes, I. S. C., Newman, J. O. H., and Bond, G. C., *Appl. Catal.* **30,** 303 (1987).
29. Rameswaran, M., and Bartholomew, C. H., *J. Catal.* **117,** 218 (1989).
30. Jones, V. K., Neubauer, L. R., and Bartholomew, C. H., *J. Phys. Chem.* **90,** 4839 (1986).
31. Rankin, J. L., and Bartholomew, C. H., *J. Catal.* **100,** 533 (1986).
32. Amelse, J. A., Butt, J. B., and Schwartz, L. H., *J. Phys. Chem.* **82,** 558 (1978).
33. Diebold, U., Pan, J.-M., and Madey, T. E., *Surf. Sci.* **287–288,** 896 (1993).
34. Diebold, U., Pan, J.-M., and Madey, T. E., *Phys. Rev. B* **47,** 3868 (1993).
35. Pan, J.-M., and Madey, T. E., *J. Vac. Sci. Technol. A* **11,** 1667 (1993).